The electronic structure and the O 1s x-ray absorption cross section of the perovskite-derived compound $SrNbO_{3.4}$

2000 J. Phys.: Condens. Matter 12 1735

(http://iopscience.iop.org/0953-8984/12/8/316)

J. Phys.: Condens. Matter **12** (2000) 1735–1751. Printed in the UK PII: S0953-8984(00)06511-5

The electronic structure and the O 1s x-ray absorption cross section of the perovskite-derived compound $SrNbO_{3.4}$

H Winter, S Schuppler and C A Kuntscher
Forschungszentrum Karlsruhe, INFP, PO Box 3640, D-76021 Karlsruhe, Germany

Received 2 August 1999, in final form 18 October 1999

Abstract. We present the results of self-consistent LMTO-ASA band structure calculations for $SrNbO_{3.4}$ based on the LDA. Eight bands per spin cut the Fermi surface. In accordance with experiment, we obtain a low density of states at the Fermi level, rising steeply with increasing energy. This explains qualitatively the low susceptibility found in this material. Similar to the simple perovskite structure $SrNbO_3$, the conduction band complex is separated from the 5.6 eV wide valence band region by a gap of 1.7 eV. The spatial charge distribution shows that the bonding between the niobium and the oxygen atoms within the two-dimensional octahedral network is of primarily ionic character. A band complex of width 3.45 eV found at 17 eV below E_F is due to the O 2s states. The reasonable agreement between our calculated XAS cross sections for different light polarizations with recent experimental results suggest that an LDA treatment of this class of substances is appropriate, whereas Coulomb correlations play a minor role.

1. Introduction

Since the discovery of the high-T_c superconductors on the basis of Cu–O building blocks, the properties of materials of similar structure where Cu is replaced by some other transition metal atom have been investigated intensively. There is a rich variety of known compounds containing Nb–O clusters. In addition, novel structures built by lower than three-dimensional networks of Nb–O entities in octahedral or prismatic coordination have been synthesized.

Superconductivity in niobium oxides at rather low temperatures has been observed only in a few cases: the layered niobium oxide phase Li_xNbO_2 has a transition at about 5 K for x near 0.5 [1], while the orthorhombic systems $Sr_{1-x}Ln_xNb_2O_{6-y}$ (Ln: La, Nd, Pr, Ce, Gd, Ho) show onsets of superconductivity at temperatures up to 12 K [2]. In fact, the ground states of the niobium oxides studied so far vary between poorly metallic, semiconducting, insulating, and ferroelectric, in many cases depending on moderate differences in the stoichiometry of oxygen or alkaline atoms stabilizing the structure.

The simplest compound in the family of Nb-based perovskites is $SrNbO_3$ [3, 4]. It crystallizes in the simple perovskite structure and is composed of a three-dimensional network of corner-sharing NbO_6 octahedra, while the Sr atoms fill the empty space in between. Turzhevsky *et al* [5] performed LDA band structure calculations for this compound using the LMTO method. They found a valence band complex of 6 eV width with significant Nb 4d–O 2p hybridisation and a considerable partial density of states (DOS) at the Sr sites. The Fermi level, E_F, is separated from those states by a 2.3 eV wide gap and is located at the shoulder of the conduction band of mainly Nb 4D character. In accordance with conclusions drawn from experiment [6], these theoretical results demonstrate that Nb is tetravalent in

0953-8984/00/081735+17$30.00

this compound. The low value for the DOS at E_F is compatible with the observed poor conductivity as well as with the low susceptibility of this material. By slightly changing the stoichiometry of Sr or O, respectively, one can tune the electrical behaviour between insulating and metallic. This observation agrees with the calculations assuming a nearly rigid band picture.

Experimental XPS and UPS valence band spectra for $SrNbO_3$ show a valence band of 6 eV width in agreement with theory [6]. The shape of the O 1s, Nb 3d, Sr 3p, and Sr 3d core-level XPS spectra in [6] for Sr_xNbO_3, with x varying between 0.8 and 0.9, do not depend significantly on the Sr stoichiometry. From these curves the authors draw the conclusion that the valence of Nb varies between 4.4 and 4.2.

More complicated are the intergrowth phases, consisting of perovskite layers with NbO_6 octahedra separated by $(NbO)_3$ layers. The latter are built by Nb_6 octahedra with coordination of four O atoms per Nb atom. While $BaNb_4O_6$ contains one perovskite layer per unit cell, in $Ba_2Nb_5O_9$ there are two of them [7]. According to theory [5], no gap between the valence bands and the conduction bands exists in these substances. They are metallic and the DOS at E_F rises steeply on increasing the number of perovskite layers per unit cell.

Applying the oxygen intercalation process, a variety of still more complex compounds has been produced [8]. In these materials the compact structures consisting of ABO_3 and $(BO)_3$ units are sliced into lower-dimensional subunits, containing well defined amounts of oxygen. The compounds described in [8] contain rare earth and titanium atoms. Especially interesting in the context of the present paper are compounds of composition $SrNbO_x$ with x ranging from 3.4 to 3.5, which have been synthesized, by applying a similar procedure [9]. For x up to 3.42 they show semiconducting behaviour with activation energies as low as a few millielectronvolts. For $x = 3.5$ they are ferroelectric, whereas for compositions between $x = 3.42$ and $x = 3.5$ well ordered intergrowth of the semiconducting and the ferroelectric phase is observed. These substances crystallize in ordered structures built up by large unit cells. In the case of $SrNbO_{3.4}$, for example, the tetragonal unit cell contains ten formula units ($Sr_{10}Nb_{10}O_{34}$) and consists of the building blocks of strongly distorted, edge sharing NbO_6 octahedra. The lattice constants are extremely anisotropic. They have the values $a = 3.995$ Å, $b = 5.674$ Å, and c(perpendicular to the slab planes) $= 32.456$ Å. The conductivity properties of this compound may be improved by substituting Sr with a higher valent element. In the case of La, the composition $La_{0.1}Sr_{0.9}NbO_{3.4}$ has been achieved [9].

Kuntscher *et al* [10] performed extensive spectroscopic experiments for this substance. The angle-resolved photoemission (ARPES) data of these authors in the near-E_F region show interesting features. For wavevectors in the $\bar{\Gamma}$–$\bar{Y}$ direction they observed two practically flat bands at 0.3 eV and 0.65 eV below E_F, but no band crossing the Fermi level. In the $\bar{\Gamma}$–$\bar{X}$ direction, on the other hand, the lower one of these bands does show dispersion, and crosses the Fermi level. These results suggest that the electronic structure within the planes perpendicular to the slab surfaces is remarkably anisotropic. Since ARPES experiments might be expected to be surface sensitive, the additional oxygen 1s x-ray absorption measurements of [10], probing bulk properties, are of great importance. In this experiment a distinct peak of width 2 eV immediately above threshold separated by deep minima from the high-energy part of the spectrum has been found. The position and height of this peak depend on the light polarization.

The goal of the present paper is to give a detailed description of the electronic structure of the stoichiometric compound $SrNbO_{3.4}$, including partial DOS, charge distributions, the character of the bands, and Fermi surface properties (section 2). In section 3 we calculate the oxygen 1s XAS cross section, to investigate if an LDA-based LMTO-ASA [11] bulk band structure calculation is able to account for the experimental results.

2. Band structure calculations

We performed self-consistent scalar relativistic LMTO-ASA band structure calculations for orthorhombic $SrNbO_{3.4}$ using the experimental atomic positions of [12] and [13]. The crystalline structure of this compound can be described as a sequence of slabs consisting of Sr, Nb, and O atoms, and stacked along the c direction. Neighbouring slabs are shifted relative to each other in the a direction by half a lattice vector. Each slab entity consists of a network of partly corner-sharing octahedra with O atoms at the corners and Nb atoms in the centres, and has an extent of five octahedra in the c direction. The space between the octahedra is filled by Sr atoms, and at the ends of the slabs, perpendicular to the c-axis, Sr sites are located at the surface. The slabs are clearly separated by interfaces where one might expect strips of low electron densities. The observed considerable and position-dependent distortion of the octahedra turns out to be an essential feature of this compound. As a consequence, the 10 Nb atoms split into three groups of sites occupying non-equivalent positions, and consisting of two, four, and four atoms each. The same is the case for the Sr atoms. The oxygen sites, on the other hand, form nine groups of non-equivalent sites, one of them containing two atoms and the others four atoms. In figure 1, we show the projections of the atomic positions into the plane of the $\boldsymbol{b}$- and the $\boldsymbol{c}$-axes. Since the non-symmorphic space group of the system is *Pnnm*, the irreducible wedge of the Brillouin zone (IRBZ) is one eighth of its total volume.

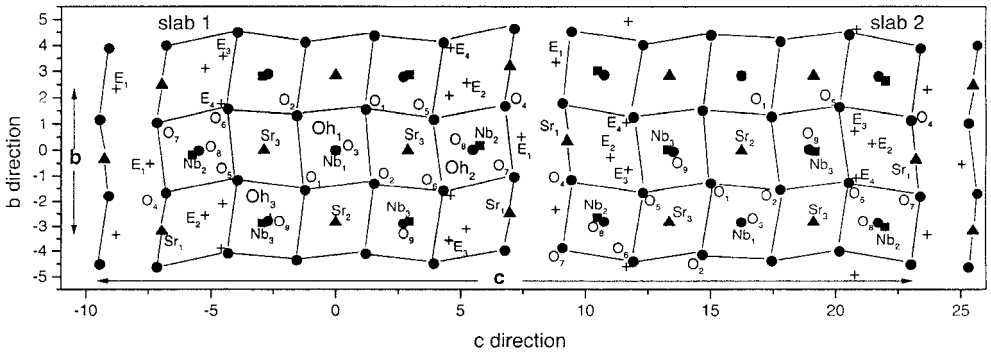

Figure 1. The projection of the atomic positions into the b–c plane. Oh_1, Oh_2, Oh_3, inequivalent octahedra; Nb_1, Nb_2, Nb_3, Nb atoms in non-equivalent positions. Sr_1, Sr_2, Sr_3, Sr atoms in non-equivalent positions; O_1, O_2, O_3, O_4, O_5, O_6, O_7, O_8, O_9, oxygen atoms in non-equivalent positions; E_1, E_2, E_3, E_4, empty spheres in non-equivalent positions.

A tetrahedron mesh of 108 $\boldsymbol{k}$-points in the IRBZ has been used in our calculations. We divided both the q_x- and the q_y-axis (lengths π/a and π/b, respectively) into six sections, whereas for the short q_z-axis (length π/c), along which hardly any band dispersion exists, three sections proved sufficient. In these two-panel calculations the lower panel comprises the Sr 4p semicore states and the O 2s states. The angular momenta include $l = 2$ at all sites. In the downfolded Hamiltonian the Nb p and the O d partial waves have been treated as intermediate waves. In addition, a total of 16 empty spheres has been inserted into the space between the slabs and the environments of the Sr atoms at the interface. Their maximum angular momentum is $l = 1$. Starting with overlapping atomic potentials, typically 60 iterations were necessary to reach convergence for the charge densities, although the typical features of the electronic structure were already showing up after a few iterations.

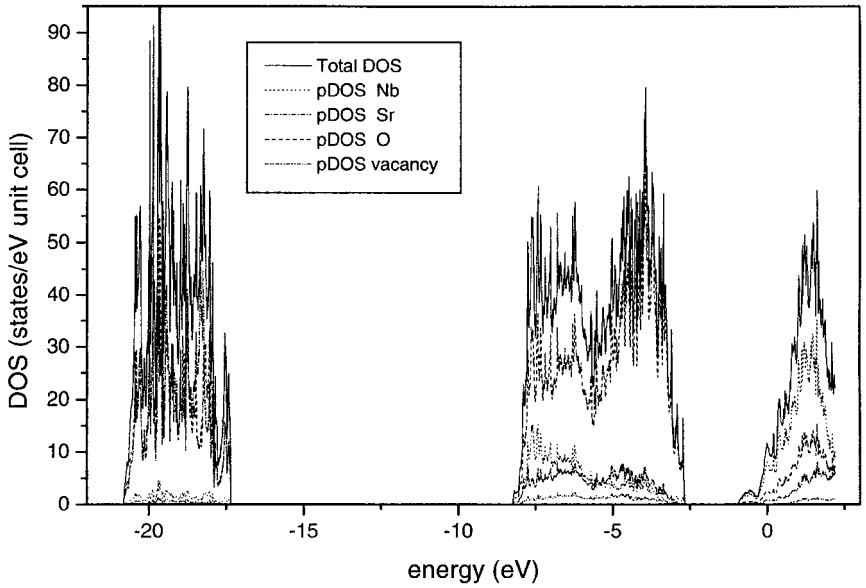

Figure 2. Total DOS for $SrNbO_{3.4}$ and DOS contributions from the Nb, Sr, and O sites.

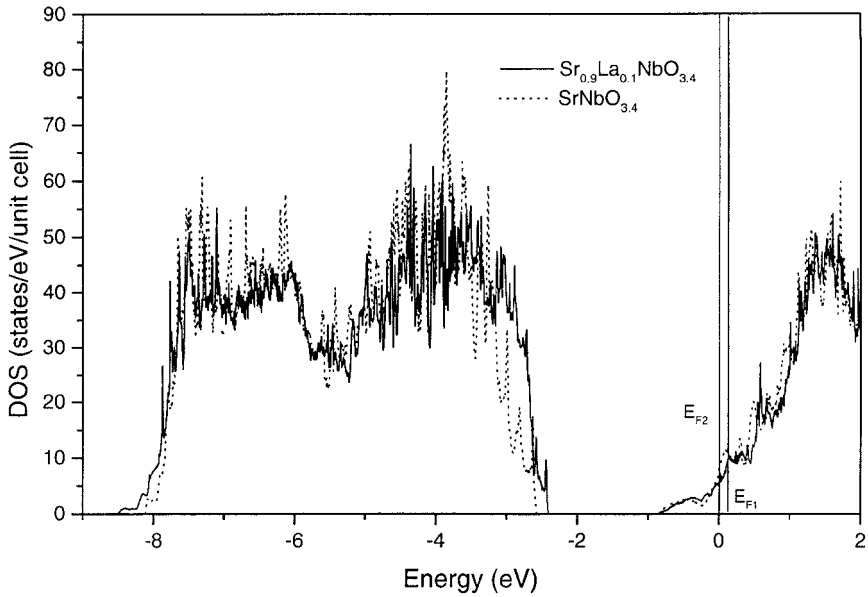

Figure 3. Comparison between the total DOS of $La_{0.1}Sr_{0.9}NbO_{3.4}$ (full curve), and $SrNbO_{3.4}$ (dotted curve). The La atoms have been put on the Sr_2 positions in slab 1 as shown in figure 1.

The total density of states, displayed in figure 2, consists of three distinct regions. The extremely narrow (width between 0.22 eV and 0.54 eV) Sr 4p and O 2s bands overlap and cover the energy range 20.81 eV to 17.27 eV below the Fermi level, E_F (capacity: 128 electrons). The second region between 8.2 and 2.57 eV below E_F consists of itinerant states built up by Sr 5s, Nb 4d, 5s, and O 2p states, and has a capacity of 204 electrons. The band widths

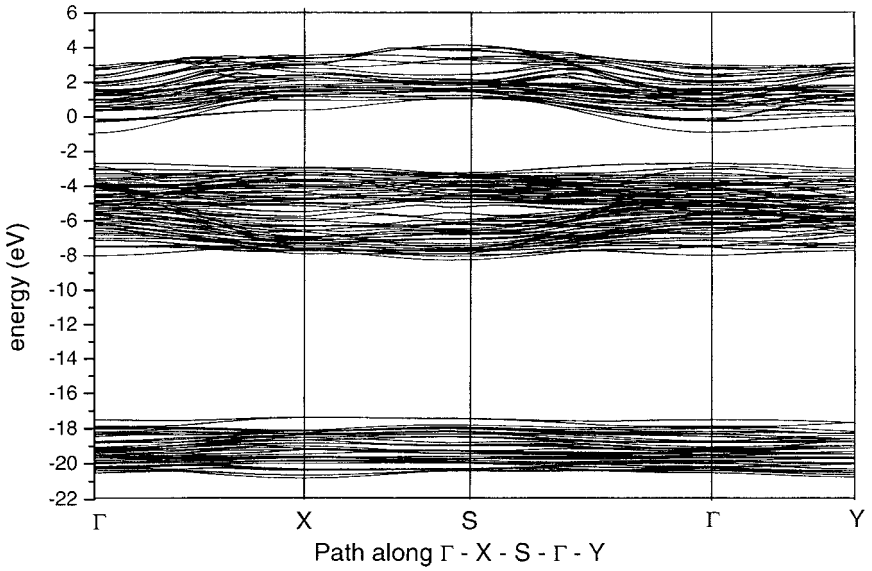

(a)

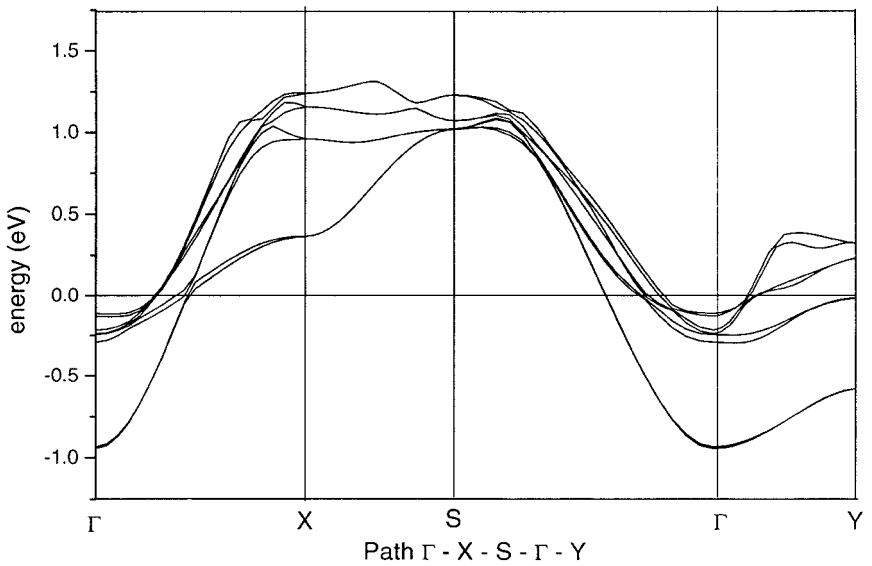

(b)

Figure 4. Bands along the path Γ–X–S–Γ–Y in the Brillouin zone. (a) Bands in an extended energy region; (b) bands cutting the Fermi level.

range from 0.4 eV to 1.34 eV. In a naïve picture one would argue that each O atom tries to fill up its 2p shell by taking two electrons from the Nb and Sr atoms. This would, in fact, correspond to the quoted capacity of this band complex and is also stressed by the fact that it is separated from the higher energy part of the spectrum by a gap of 1.7 eV width. However, as the partial densities of states (PDOS) also drawn in figure 2 show, there are still finite densities of s and d electrons mainly in the ASA spheres of the Nb atoms, but also at the Sr sites. Going further up in energy, bands start to reappear at 0.94 eV below E_F, and for the DOS

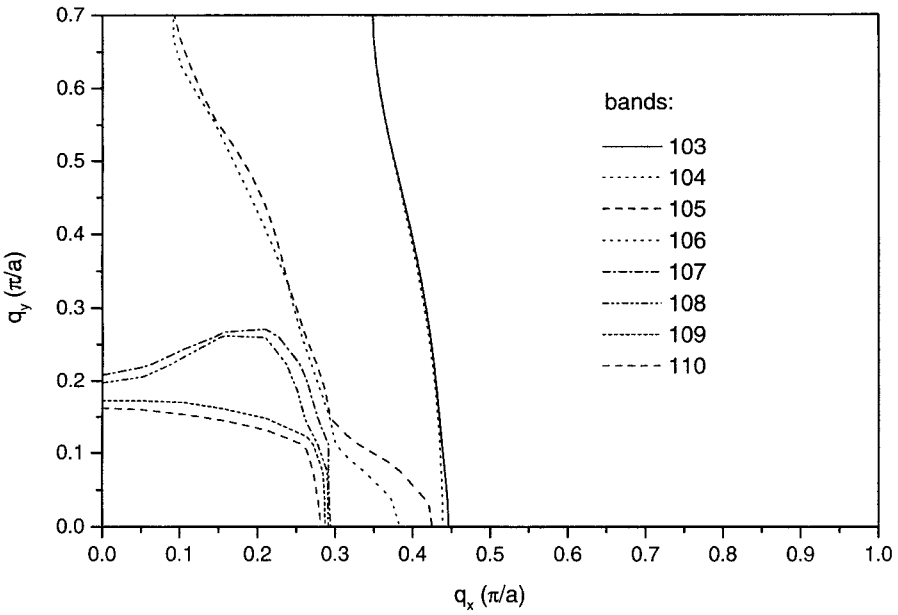

Figure 5. Cut of the Fermi surface with the q_x–q_y plane of the Brillouin zone.

at E_F we find the rather low value 8.06 (states/(eV unit cell)). On increasing energy, the Sr contribution to the characters of the states becomes more and more significant. An observation important for the O 1s x-ray absorption cross section is that the O 2p contribution is still non-negligible. Eight bands per spin cross the Fermi level, and they are partly occupied by the two electrons per unit cell not consumed in filling up the O 2p shells. Throughout the occupied part above the gap the DOS is rather small. This is the case despite the fact that these bands are still not overly wide (between 1.45 eV and 2.08 eV), since on the average they are considerably flatter in the unoccupied region than in the occupied part. At the energy 0.23 eV other bands start to overlap these eight bands and in the whole energy region of the latter the number of these bands amounts to 21 per spin. In the case of the La-doped substance $La_{0.1}Sr_{0.9}NbO_{3.4}$, used in the XAS experiments of [10], the extra electrons introduced by La, assuming rigid band behaviour, shift the Fermi energy by 0.102 eV and increase the DOS at E_F to 11.15 states/eV unit cell. This rigid band assumption is supported by supercell bandstructure calculations for $Sr_{1-x}La_xTiO_3$ with $x = 0.125$, 0.25, and 0.375, where the La atoms replace the Sr atoms at various sites [14]. We performed an additional calculation for the composition of $La_{0.1}Sr_{0.9}NbO_{3.4}$, putting the La atom on the Sr_2 site in slab 1 (see figure 1) as an example. The resulting DOS curve (figure 3) also suggests an approximately rigid band behaviour.

Figure 4(a), displaying the dispersions of the 64 semicore, the 102 bonding and 48 of the non-bonding bands per spin along the principal path in the BZ, and figue 4(b), picking up the eight bands per spin crossing the Fermi surface, illustrate these features. Since, in the region considered, the band energies do not significantly depend on q_z, these pictures are representative for the whole BZ. Figure 4(b) clearly demonstrates that there is considerable anisotropy concerning the wavevector dependence of the near-E_F bands.

The Fermi surface topology is shown in figure 5, displaying the cuts of the FS with the q_x–q_y plane of the BZ. Whereas the pairwise almost degenerate bands 103 to 106 give rise to

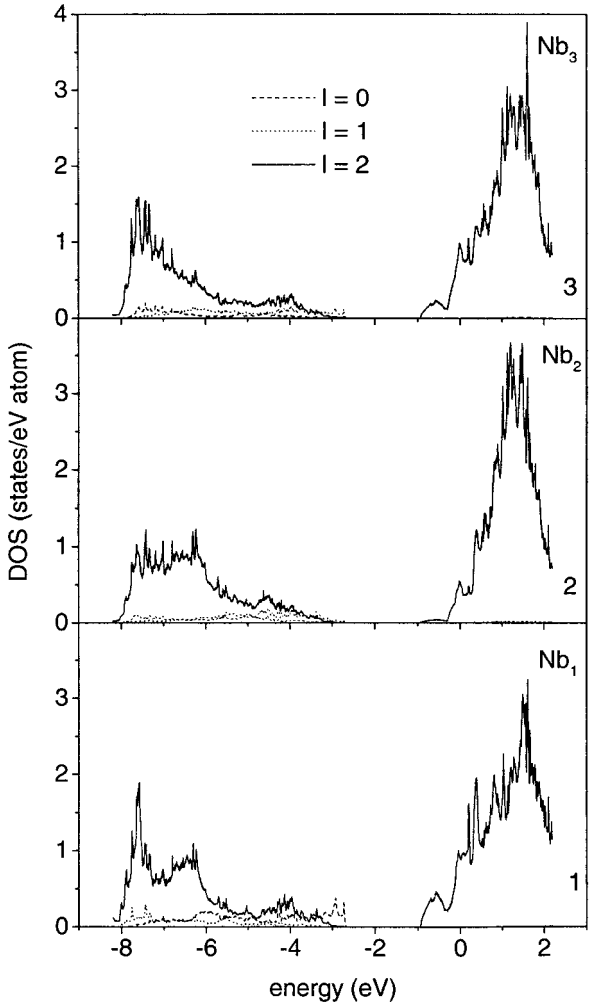

(a)

Figure 6. Angular momentum resolved partial DOS of individual atoms. (a) Nb atoms in non-equivalent positions, i.e. Nb_1 in Oh_1 (curve 1), Nb_2 in Oh_2 (curve 2), and Nb_3 in Oh_3 (curve 3). (b) Oxygen atoms in non-equivalent positions, i.e. corner atoms O_1 and O_2 in Oh_1 (curves 1 and 2), corner atoms O_4, O_5, O_6, and O_7 in Oh_2 (curves 4, 5, 6, and 7), corner atoms O_1, O_2, O_5, and O_6 in Oh_3 (curves 1, 2, 5, and 6), apical atoms O_3 in Oh_1 (curve 3), O_8 in Oh_2 (curve 8), and O_9 in Oh_3 (curve 9). (c) Sr atoms in non-equivalent positions, i.e. slab interface atoms Sr_1 (curve 1), atoms between Oh_1 and Oh_3 octahedra (Sr_2 (curve 2)), atoms between Oh_1, Oh_2, and Oh_3 octahedra (Sr_3 (curve 3)). (d) Empty spheres sites in non-equivalent positions, i.e. space between the slabs (E_1, curve 1), near-interface space between octahedra (E_2, curve 2; E_3, curve 3; and E_4, curve 4).

almost flat sheets, bands 107 to 110 create strongly deformed tubes. Due to sections in the BZ with extremely small dispersion—especially of the latter group of bands—the detailed shape of these curves is rather sensitive to the precise position of E_F.

In figure 6, we display the angular momentum resolved DOS of the different atoms in inequivalent positions. They may be interpreted in the following way. The unit cell contains three inequivalent and therefore differently distorted Nb–O octahedra Oh_1, Oh_2, and Oh_3,

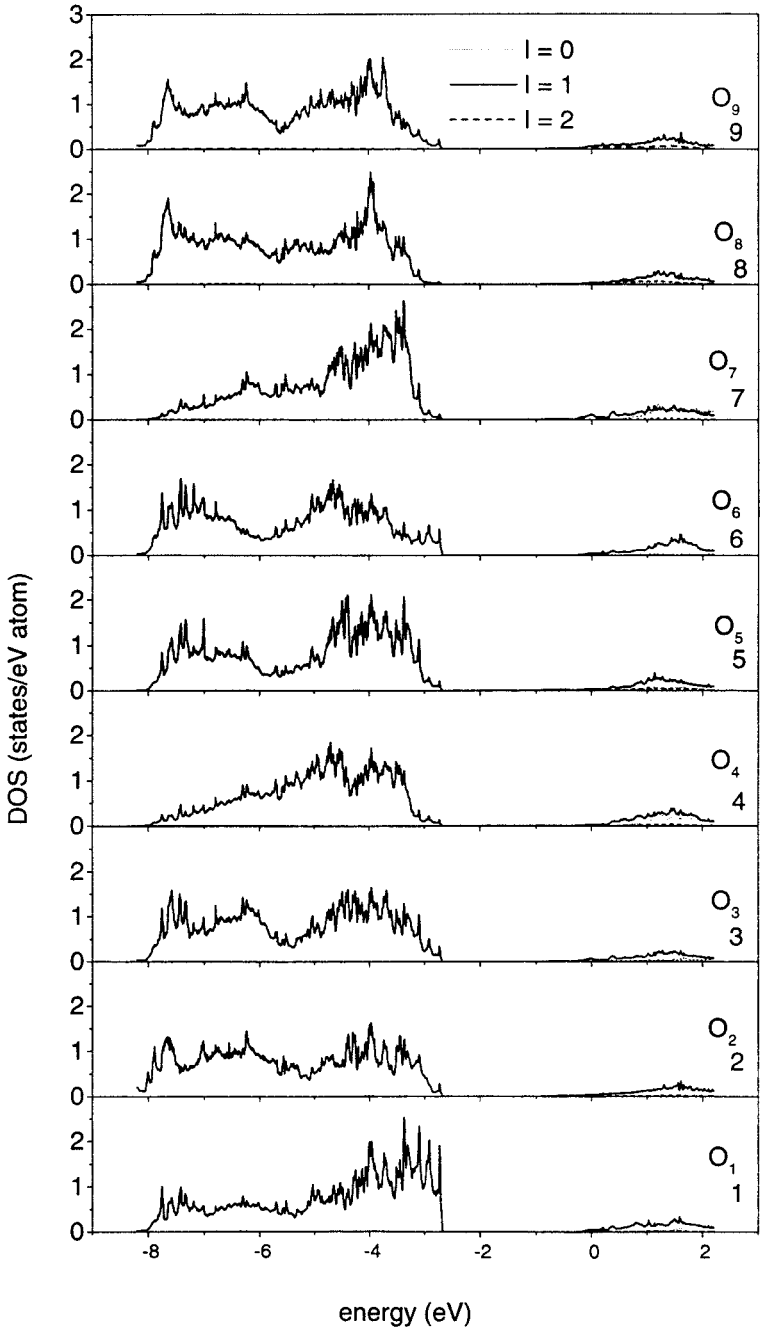

(b)

Figure 6. (Continued)

occurring with the multiplicities two, four, and four, respectively (see figure 1). According to the data given in [12] and [13], the Nb–O distances in Oh_1 vary between 1.973 and 2.034 Å

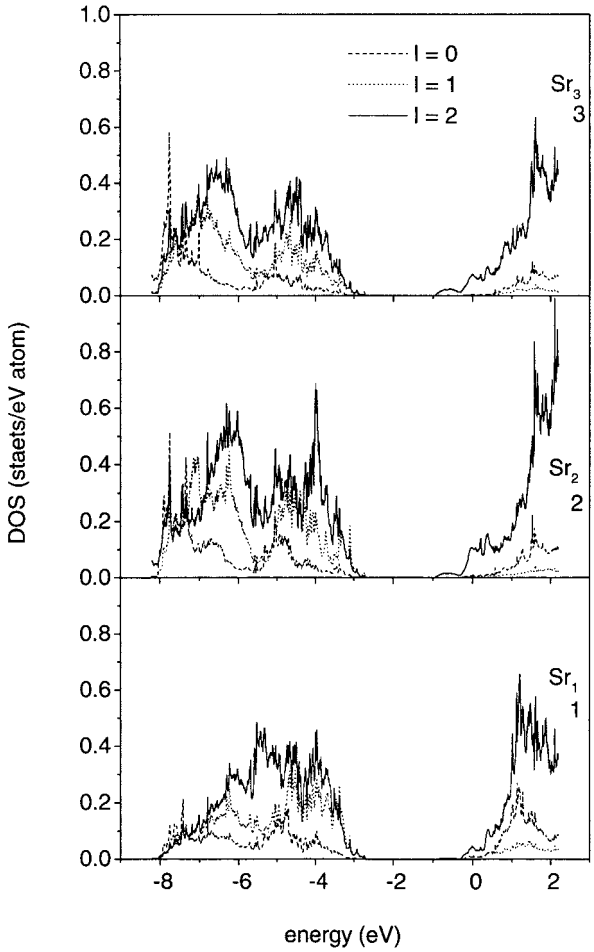

(c)

Figure 6. (Continued)

and the angles between neighbouring Nb–O directions in the oxygen plane amount to 87.86° and 92.14°, respectively. The angle between the oxygen plane and the direction along the niobium and the apical oxygen (O_3, O_8, and O_9 in figure 1) is 90°. Significantly larger are the deviations from the shape of an ideal octahedron in the case of the other types of Nb–O clusters. The corresponding numbers for Oh_2 octahedra are 1.814 to 2.022 Å, 78.98° to 96.98°, and 81.09°, respectively. For the Oh_3 type of octahedra the values are 1.842 to 2.012 Å, 82.96° to 101.92°, and 83.07°. As a consequence, there are three inequivalent Nb sites, and this is clearly demonstrated by the variances in the PDOS curves of figure 6(a). Especially pronounced are the differences in the energy region immediately below E_F, where the contribution is maximum for Nb atoms in the middle of the slabs (Nb_1 in figure 1). The PDOS are dominated by the d contributions, while the s and p contributions turn out to be rather insignificant. We observe that the Nb PDOS assume larger values in the non-bonding regime above E_F than in the bonding region. This suggests that a considerable charge transfer from niobium to oxygen has occurred. The different PDOS curves in figure 6(b) correspond to the nine inequivalent positions of the O atoms: curves 3, 8 and 9 refer to the apical oxygen atoms of Oh_1, Oh_2,

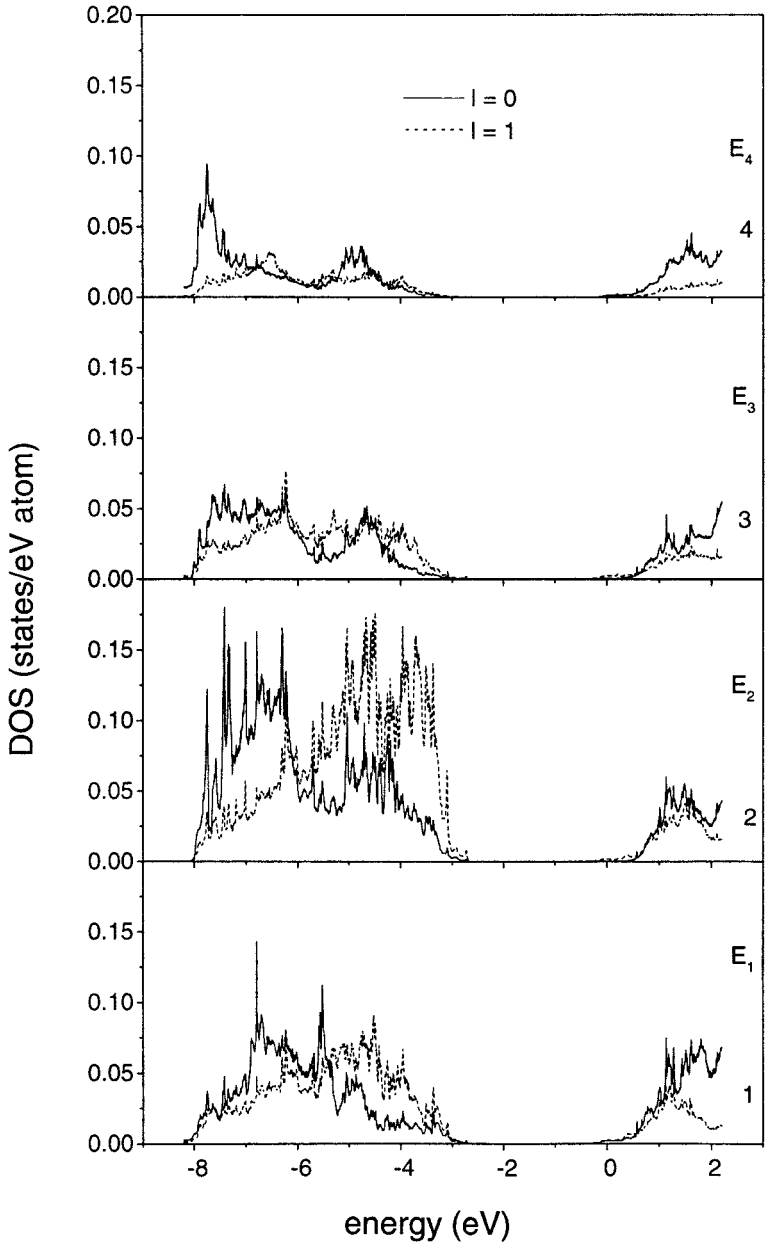

(d)

Figure 6. (Continued)

and Oh_3, respectively. The rest of the oxygen atoms correspond to the PDOS curves in the following way: Oh_1, located in the centre of the slab between its interfaces, has two pairs of non-equivalent oxygen basis atoms (O_1 and O_2 in figure 1), giving rise to curves 1 and 2. The PDOS of the two corners of Oh_2 at the slab interface (O_4 and O_7 in figure 1) are shown in curves 4 and 7. Curves 5 and 6 are due to the remaining two Oh_2 O atoms (O_5 and O_6 in

figure 1). This means that all Oh_2 O basis atoms are in non-equivalent positions. Oh_3, finally, shares two corners with octahedra of type Oh_1 (curves 1 and 2) and two corners with octahedra of type Oh_2 (curves 5 and 6). Therefore, all basis O atoms of Oh_3 are in non-equivalent positions as well. For all oxygen atoms, the p contribution dominates in the bonding region, whereas above the gap the oxygen PDOS values are rather small. The Sr atoms fall into three groups of atoms in non-equivalent positions (figure 6(c)). Curve 1 exhibits the PDOS due to the Sr interface atoms (Sr_1 in figure 1). It is distinctly different from curves 2 and 3, referring to the Sr atoms (Sr_2 and Sr_3 in figure 1) filling the space between the octahedra within the slab. The Sr_2 atoms (curve 2) are surrounded by Oh_1 as well as Oh_3 octahedra, whereas the neighbourhood of the Sr_3 atoms (curve 3) contains all three different types of octahedra. The largest contribution to the PDOS comes from the d waves in all three cases, and above E_F the Sr DOS rises fast on increasing energy. The PDOS provided by the empty spheres (figure 6(d)) finally show that the charge density in the interface near regions between the octahedra (curves 2 to 4 referring to the sites E_2, E_3, and E_4 in figure 1) is rather low and is still more depressed in the area separating two adjacent slabs (curve 1 corresponding to the sites E_1 in figure 1).

In spite of the fact that the perovskite-like structure and the octahedral building blocks of $SrNbO_{3.4}$ are reminiscent of some high-T_c materials or their parent compounds, the electronic properties of the niobates are drastically different from those of the cuprates. This may clearly be seen by considering the character of the Nb–O bonding. In figure 7, we draw the charge density profiles due to the p states at the O sites and due to the p as well as the d states at the Nb sites along the lines connecting the Nb with the O atoms within the three non-equivalent octahedra. Noticing the substantial variations of the Nb–O distances, these pictures again visualize the considerable distortions of the octahedra, strongest for types Oh_2 and Oh_3, since they contain oxygen atoms in the vicinity of the slab interfaces. As a common feature, however, we observe low charge densities in extended regions between the Nb and the neighbouring O atoms. The broad peak at the oxygen site, caused by states of p character, demonstrates that considerable charge transfer from Nb to O has occurred and that the bonding is mainly of ionic nature. The Nb 5s contribution, not displayed in figure 7, is not significant and does not change this picture, while the O 2s electrons are entirely localized at the O sites in the compound. Moreover, as figure 6 points out, the centres of gravity of the Nb d states, on the other hand, and of the O p states, on the other, have markedly different energies.

Since the near-E_F bands are important for the interpretation of angle-resolved photoemission (ARUPS) experiments and also for the dc conductivity, it is worth describing their character in more detail. In table 1 we list the charge distributions due to bands 103 to 110 (counted from the bottom of the non-zero DOS region above the semicore states) in the ASA spheres of the individual atoms in the unit cell averaged over the $\boldsymbol{k}$-points of the BZ in the occupied region. Between 65% (band 109) and 74% (band 103) of the charge, practically entirely of d character, is sitting at the Nb sites, and 19% (band 103) to 25% (band 110) at the O sites with mainly p character but non-negligible d and s contributions. The share of the Sr atoms lies between 6.4% (band 103) and 8.7% (band 109) and is of predominantly d character. The charge in the empty spheres turns out to be negligible. The numbers given above mean that these states are not localized but have appreciable amplitudes throughout the unit cell in both of the slabs displaced relative to each other. A qualitatively similar picture results if we average over the $\boldsymbol{k}$-points along the $\bar{\Gamma}$–$\bar{X}$ or the $\bar{\Gamma}$–$\bar{Y}$ direction. This should be kept in mind if one tries to interpret the ARUPS experiments of [10] in terms of the bulk band structure. These experiments investigate the electronic structure of a crystal cleaved perpendicular to the $\boldsymbol{c}$-axis, most probably at the interface of two slabs. If in the region near to the interface one of the slabs

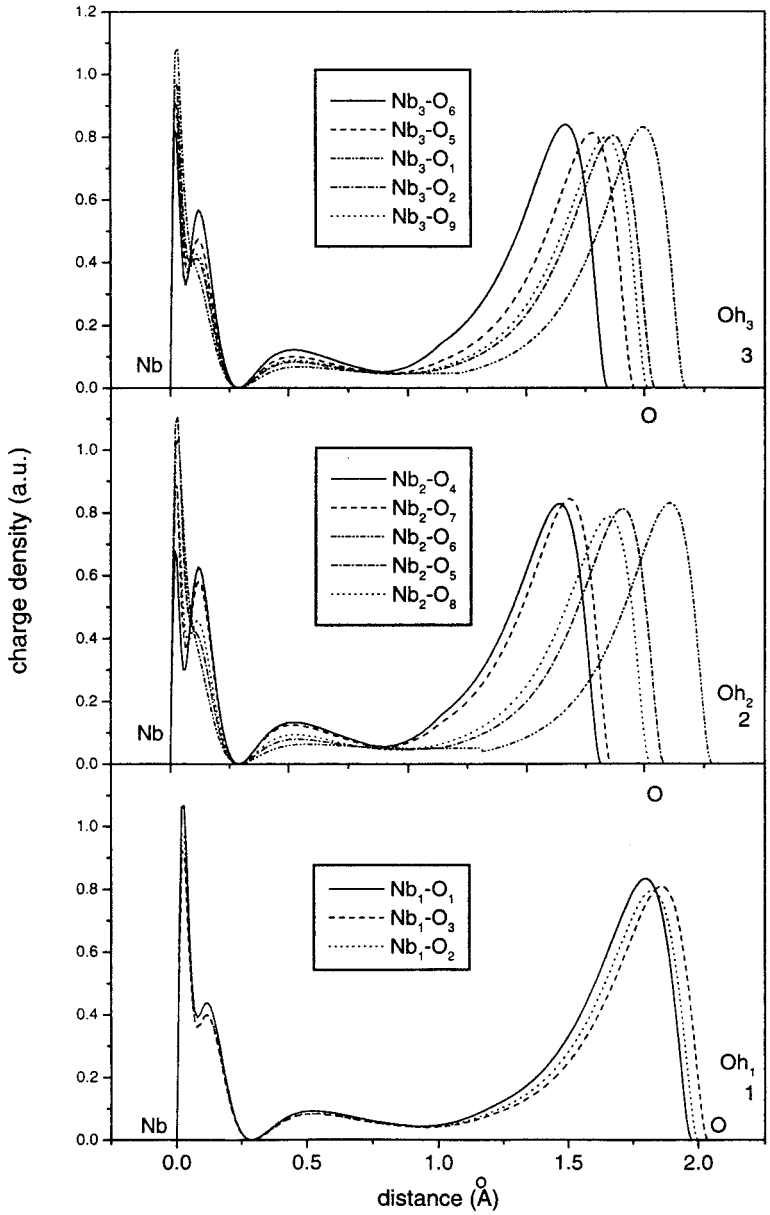

Figure 7. Charge densities along the Nb–O directions in the octahedra, i.e. in Oh_1 (curve 1), Oh_2 (curve 2), and Oh_3 (curve 3).

is missing, the charges must rearrange and the corresponding states might therefore change, influencing the results of the ARUPS measurements. In addition, due to scattering processes of the excited electrons, the extraction depth of the electrons is limited, and also matrix element effects might be important. The LDA calculations for the bulk reproduce, however, one important experimental result: the dispersion of the near-E_F bands is significantly smaller in the Γ–Y than in the Γ–X direction.

Table 1. The charge distribution due to the near-E_F bands in the ASA spheres of the individual atoms, averaged of the $\boldsymbol{k}$-points in the occupied region.

Type of atoms	Bands							
	103	104	105	106	107	108	109	110
Nb_1	0.3238	0.3251	0.0669	0.0589	0.2840	0.2824	0.2875	0.2455
Nb_2	0.0713	0.0683	0.2593	0.2492	0.0978	0.0850	0.1744	0.3065
Nb_3	0.3458	0.3461	0.3797	0.3906	0.3000	0.3134	0.1908	0.1161
Sr_1	0.0106	0.0106	0.0307	0.0307	0.0137	0.0116	0.0256	0.0309
Sr_2	0.0128	0.0128	0.0147	0.0149	0.0397	0.0377	0.0331	0.0243
Sr_3	0.0404	0.0405	0.0262	0.0272	0.0329	0.0333	0.0290	0.0215
O_1	0.0030	0.0030	0.0103	0.0103	0.0524	0.0541	0.0532	0.0344
O_2	0.0321	0.0324	0.0405	0.0424	0.0189	0.0209	0.0340	0.0346
O_3	0.0254	0.0256	0.0045	0.0042	0.0107	0.0108	0.0089	0.0095
O_4	0.0017	0.0019	0.0085	0.0086	0.0102	0.0097	0.0149	0.0201
O_5	0.0407	0.0412	0.0241	0.0252	0.0111	0.0139	0.0193	0.0137
O_6	0.0058	0.0058	0.0127	0.0126	0.0332	0.0336	0.0290	0.0187
O_7	0.0232	0.0233	0.0699	0.0730	0.0203	0.0182	0.0442	0.0636
O_8	0.0156	0.0156	0.0251	0.0257	0.0181	0.0186	0.0154	0.0223
O_9	0.0454	0.0455	0.0234	0.0233	0.0527	0.0526	0.0342	0.0357
E_1	0.0006	0.0006	0.0018	0.0013	0.0012	0.0007	0.0030	0.0013
E_2	0.0004	0.0004	0.0006	0.0008	0.0008	0.0009	0.0017	0.0004
E_3	0.0010	0.0011	0.0007	0.0008	0.0015	0.0018	0.0011	0.0007
E_4	0.0002	0.0002	0.0003	0.0003	0.0007	0.0007	0.0008	0.0004

Finally, we emphasize that the distortions of the octahedra are essential for the peculiar electronic properties of $SrNbO_{3.4}$, i.e. an energy gap in the occupied region and a low DOS at the Fermi level: LMTO-ASA calculations for a hypothetical structure where the Nb atoms of Oh_2 and Oh_3 have been displaced artificially by 0.31 Å and 0.22 Å, respectively, to bring these atoms into more symmetric positions, yield a band structure (not shown in this paper) without any gap and a relatively high DOS value at E_F. The distortions observed in the real structure, however, are not the result of an electronic instability created to lower the electronic energy of the system, but rather a consequence of the stoichiometry of this compound, not allowing the formation of just one type of corner-sharing octahedron. The differences in the environment of the oxygen atoms therefore lead to the distortions of the octahedra and, as a consequence, to the peculiar electronic structure of $SrNbO_{3.4}$.

In [10], which is mainly devoted to experiment, a total DOS curve as well as dispersions of the near-E_F bands are shown. These results originate from a band structure calculation based on pseudopotentials. Since this method is rather laborious, it is gratifying to observe that the electronic structure of $SrNbO_{3.4}$ presented in this paper and gained by applying the simpler and much more rapid LMTO-ASA calculations, shows reasonable agreement. This statement refers to the fact that both methods find three groups of bands clearly separated by energy gaps: the low-lying, O 2s dominated band complex, the intermediate region of mainly O 2p character, and the high-energy part where the Sr contributions become more and more significant. The disappearance of the higher energy gap on shifting the Nb atoms is also a common finding, as well as the observed anisotropy of the near-E_F bands as a function of the direction of the $\boldsymbol{k}$-vector in the slab. There are of course some quantitative differences, for example, the width of the higher energy gap, which is 1.7 eV in the LMTO-ASA case as compared to 1.1 eV in the pseudopotential case. We also observe variances in the details of the near-E_F bands. However, they cannot be contrasted to the ARPES experiments of [10], since the interpretation of these measurements requires layer calculations.

3. The oxygen 1s XAS cross section

The O 1s and the Nb 2p core levels are the most obvious choices for investigating the electronic structure close to E_F in near-edge XAS. While the Nb p core states are strongly lifetime broadened ($\sim$ 2 eV), the broadening of the oxygen 1s core level at -543 eV amounts to only $\sim$ 0.2 eV [15, 16]. The XAS experiments for $La_{0.1}Sr_{0.9}NbO_{3.4}$ of [10] performed for light polarizations $\boldsymbol{E}$ parallel to the crystallographic $\boldsymbol{a}$-, $\boldsymbol{b}$-, as well as $\boldsymbol{c}$-axes yield a distinct, approximately 1 eV, wide peak at the onset of the spectrum, followed by a marked dip and a steep rise of the cross section towards higher energies. The onset of the peak belonging to light polarization parallel to $\boldsymbol{a}$ precedes the others by about 0.3 eV and the peak amplitude is enhanced by 30–40%.

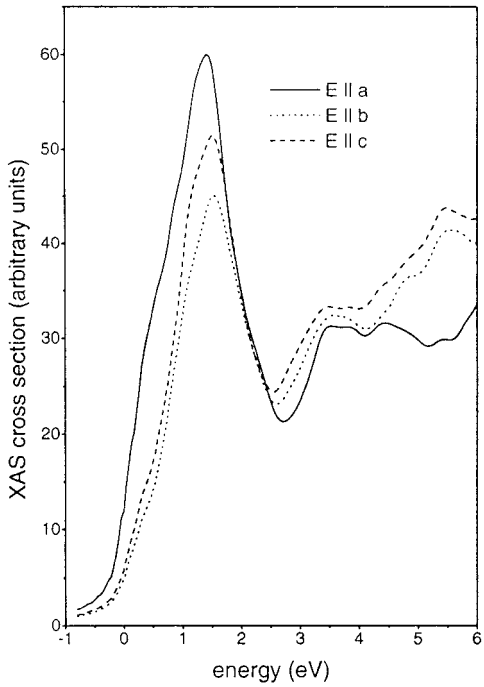

Figure 8. The O 1s XAS cross sections, calculated for light polarizations oriented along the crystallographic axes.

The lowest order Feynman diagram, renormalized with respect to the electron propagators, yields the following expression for the cross section when a core hole with the principal quantum number n, and the angular quantum numbers j, μ, and l_c is created at site τ:

$$\sigma(\omega;\nu) \propto \sum_{\lambda} \int \mathrm{d}\boldsymbol{k}/\Omega_{BZ} \int \mathrm{d}\varepsilon |M_{\nu,\lambda}|^2 A_{\tau}^{(c)}(\varepsilon) A_{\lambda}(\boldsymbol{k};\varepsilon+\omega) f(\varepsilon)(1-f(\varepsilon+\omega)). \tag{1}$$

Here, the spectral function, $A_{\tau}^{(c)}$, of the core hole at energy ε_c and of width Γ_c, and the spectral function, A_{λ}, of the excited electron with Bloch vector $\boldsymbol{k}$ in band λ (energy $E_{\boldsymbol{k}\lambda}$, lifetime $1/\Gamma_{\boldsymbol{k},\lambda}$), respectively, are given by the following expressions:

$$A_{\tau}^{c}(\varepsilon) = \frac{1}{\pi}\Gamma_c/[(\varepsilon-\varepsilon_c)^2+\Gamma_c^2] \qquad A_{\lambda}(\boldsymbol{k};\varepsilon+\omega) = \frac{1}{\pi}\Gamma_{\boldsymbol{k},\lambda}/[(\varepsilon+\omega-E_{\boldsymbol{k},\lambda})^2+\Gamma_{\boldsymbol{k},\lambda}^2]. \tag{2}$$

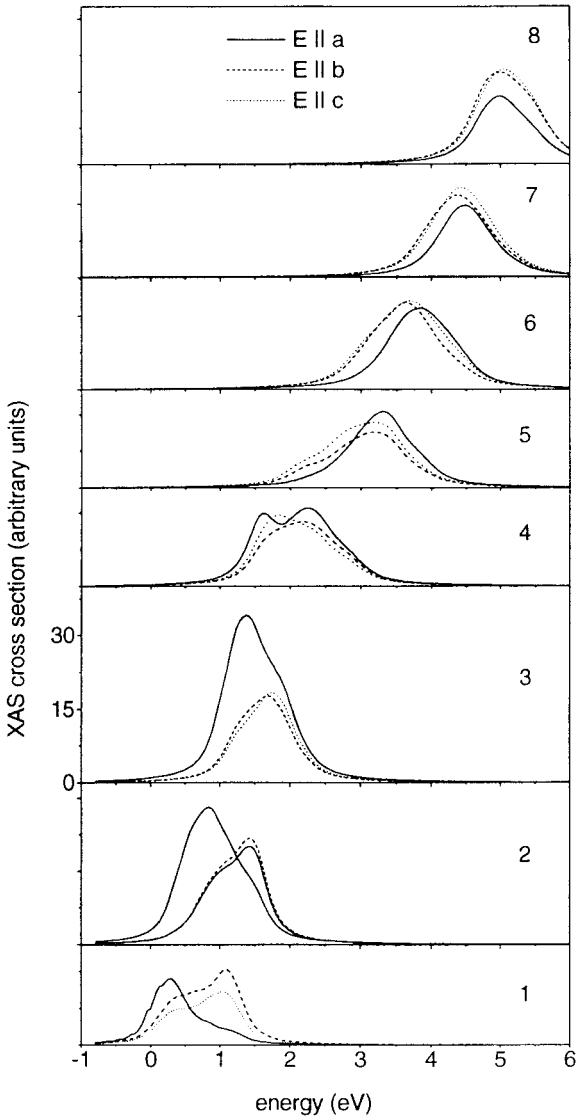

Figure 9. Contributions of transitions into individual groups of bands to the XAS cross section, i.e. into bands 103 to 110 (curve 1), bands 111 to 120 (curve 2), bands 121 to 130 (curve 3), bands 131 to 140 (curve 4), bands 141 to 150 (curve 5), bands 151 to 160 (curve 6), bands 161 to 170 (curve 7), and bands 171 to 180 (curve 8).

The matrix element, $M_{v,\lambda}$, is given by the following formula:

$$M_{v,\lambda} = \omega^{-1/2} \int \mathrm{d}\boldsymbol{\rho}\, \Phi^*_{c,\tau}(\boldsymbol{\rho}) e_v \nabla \boldsymbol{\rho} \psi_{\boldsymbol{k},\lambda}(\boldsymbol{\rho}) = \sqrt{(4\pi/3)} \sum_{m_s} C(j, \mu; l_c, \mu - m_s; 1/2, m_s)$$
$$\times \sum_{m,\kappa} [G(l_c + 1, m; l_c, \mu - m_s; 1, m_p) a_{l_c+1,m,\tau;\kappa;\boldsymbol{k}} I^{(+)}_{\kappa}$$
$$+ G(l_c - 1, m; l_c, \mu - m_s; 1 m_p) a_{l_c-1,m,\tau;\kappa;\boldsymbol{k}} I^{(-)}_{\kappa}]. \qquad (3)$$

Here, $\boldsymbol{e}_v$ is the light polarization vector, m_p assumes the values -1, 0, 1, depending on the Cartesian components of $\boldsymbol{e}_v$ and C and G denote Clebsch–Gordan coefficients and Gaunt numbers. The Bloch states, $\psi_{\boldsymbol{k},\lambda}$, are represented in the well known form of the LMTO-ASA method:

$$\psi_{\boldsymbol{k},\lambda}(\boldsymbol{\rho},\tau) = \sum_{l,m,\kappa} a_{l,m,\tau;\kappa;\boldsymbol{k}} R_{l,\kappa,\tau}(\rho) Y_{l,m}(\boldsymbol{\rho}). \tag{4}$$

$I^{(+,-)}$, finally are the following radial integrals:

$$\begin{aligned} I_\kappa^{(+)} &= \int \mathrm{d}\rho\, \rho^2 R^{(c)}_{n,j,l_c,\kappa;\tau}(\rho)[(l_c+2)R_{l_c+1,\kappa,\tau}(\rho)/\rho + R'_{l_c+1,\kappa,\tau}(\rho)] \\ I_\kappa^{(-)} &= \int \mathrm{d}\rho\, \rho^2 R^{(c)}_{n,j,l_c,\kappa;\tau}(\rho)[-(l_c-1)R_{l_c-1,\kappa,\tau}(\rho)/\rho + R'_{l_c-1,\kappa\tau}(\rho)]. \end{aligned} \tag{5}$$

Equations (1)–(5) clearly exhibit the dipole selection rule, $l = l_c \pm 1$, and in the case of the oxygen 1s core-level, where only the first term survives, the oxygen p_x, p_y, or p_z character of the excited states is probed, depending on the direction of the photon polarization vector, $\boldsymbol{e}_v$. It may be of interest to add a remark on performing the BZ integration in equation (1). Inserting the expressions for the spectral functions, (2), into (1), the following energy integral, I, occurs in equation (1):

$$I = \int_{-E_{exc}}^{|\varepsilon_c|} \mathrm{d}y \frac{1}{[y^2+\Gamma_c^2]} \frac{1}{[(y+E_{exc}-(E_{\boldsymbol{k},\lambda}-E_F))^2+\Gamma^2_{\boldsymbol{k},\lambda}]} = z(E_{\boldsymbol{k},\lambda}, E_{exc}) \tag{6}$$

with $E_{exc} = \omega + \varepsilon_c - E_F$. Due to the sizeable value of Γ_c, this function is sufficiently broad to allow for evaluating the BZ integral by sampling.

The XAS cross section, shown in figure 8, has been obtained by evaluating equations (1)–(4) using the LDA-LMTO-ASA band structure discussed in the preceding chapter. For the core level broadening, Γ_c, we chose the value 0.2 eV. For $\Gamma_{\boldsymbol{k},\lambda}$ we assumed

$$\Gamma_{\boldsymbol{k},\lambda} = \alpha(E_{\boldsymbol{k}\lambda} - E_F)^2 \tag{7}$$

with $\alpha = 0.003\ \mathrm{eV}^{-1}$. The shape of the cross section turned out to be rather insensitive to the precise form of $\Gamma_{\boldsymbol{k},\lambda}$. The theoretical cross section describes the main features of the experiment. We find a pronounced peak immediately above the Fermi energy, and the curve corresponding to a light polarization parallel to the $\boldsymbol{a}$-axis starts at lower energies than the curves for $\boldsymbol{E} \parallel \boldsymbol{b}$ and $\boldsymbol{E} \parallel \boldsymbol{c}$. The amplitude of the first-mentioned curve is highest, and a minimum in the cross section separates these FS near peaks from the higher energy parts. In spite of the fact that there are some quantitative differences between theory and experiment (magnitude of the dip between the near-E_F part and the higher energy part of the XAS cross section, which is more pronounced in the experiment, ratio of the peak heights for $\boldsymbol{E} \parallel \boldsymbol{b}$ and $\boldsymbol{E} \parallel \boldsymbol{c}$), the agreement is satisfactory and supports our band structure results. One should keep in mind that the present theory for the XAS cross section ignores all higher-order Feynman diagrams. As figure 9 shows, the low-energy peak in the XAS cross section is not mainly the result of transitions into the unoccupied parts of the eight bands per spin cutting the FS (figure 9, curve 1). The main contributions are rather due to bands 111 to 120 (figure 9, curve 2), and bands 121 to 130 (figure 9, curves 3).

4. Conclusions

Our LMTO band structure results for this complicated oxygen intercalated system show surprising similarities with the electronic structure of the three-dimensionally interconnected compound $SrNbO_3$ [5], with respect to the width of the valence band, the existence of a

sizeable gap between the valence band and the conduction band, and a low DOS at the Fermi level rising steeply with increasing energy. As a consequence of the reduced dimensionality of the $SrNbO_{3.4}$ system, however, the bands turn out to be two-dimensional, showing a very weak dispersion in the q_z direction. The main features of the electronic structure of this compound can be understood by simply assuming that oxygen catches two electrons from the earth alkali and the transition metal atoms to achieve bonding within the octahedral network, and our analysis of the spatial charge distribution between Nb and the O atoms reveals the predominantly ionic character of this bonding. The remaining two electrons per unit cell fill the low DOS shoulder of the conduction band, consisting of eight bands per spin cutting the Fermi surface. Due to the low DOS at E_F, theory predicts low susceptibility values in accordance with experiment. The poor conductivity of this compound can be qualitatively traced back to the low density of conduction electrons. However, a detailed study would be necessary to reveal the nature of the perturbations leading to the observed finite activation energies and the processes assisting the mobility of the electrons. In any case, the causes for these phenomena are not tiny gaps in the bulk electronic structure.

Our theory for the oxygen 1s x-ray absorption cross section, based on the lowest order Feynman diagram and lifetime broadened propagators, reproduces all the principal features of the experimental curve, including the shift of the onset for $\boldsymbol{E} \parallel \boldsymbol{a}$ polarization to lower energies. We have shown that the low-energy peak is not mainly caused by the eight bands per spin crossing the Fermi surface, but predominantly by the 20 following bands, overlapping the former in parts of the Brillouin zone. The observed positional dependence of the low-energy shoulders of the peaks on light polarization is not an indication of pronounced anisotropies of the bulk near-E_F bands with respect to the direction of the $\boldsymbol{q}$ vector parallel to the interfaces of the slabs.

References

[1] Geselbracht M J, Richardson T J and Stacy A M 1990 *Nature* **345** 324
[2] Akimitsu J, Amano J, Sawa H, Nagase O, Gyoda K and Kogai M 1991 *Japan. J. Appl. Phys.* **30** L1155
[3] Ridgley D and Ward R 1955 *J. Am. Chem. Soc.* **77** 6132
[4] Kreiser R and Ward R 1970 *J. Solid State Chem.* **1** 368
[5] Turzhevsky S A, Novikov D L, Gubanov V A and Freeman A J 1994 *Phys. Rev.* B **50** 3200
[6] Isawa K, Itti R, Sugiyama J, Koshizuka N and Yamauchi H 1994 *Phys. Rev.* B **49** 3534
[7] Swensson G 1989 *Solid State Ionics* **32/33** 126
[8] Bednorz J G, Wachtmann K H, Broom R and Ariosa D 1997 *High-T_c Superconductivity 1996: Ten Years after the Discovery* ed E Kaldis *et al* (Dordrecht: Kluwer) p 95
[9] Lichtenberg F, Williams T, Reller A, Widmer D and Bednorz J G 1991 *Z. Phys.* B **84** 369
[10] Kuntscher C A, Gerhold S, Nücker N, Cummins T R, Lu D-H, Schuppler S, Gopinath C S, Lichtenberg F, Mannhart J and Bohnen K-P *Phys. Rev.* B, to appear
[11] Andersen O K 1975 *Phys. Rev.* B **12** 864
[12] Schmalle H W, Williams T and Reller A 1992 *Acta Crystallogr.* C **51** 1243
[13] Abrahams S C, Schmalle H W, Williams T, Reller A, Lichtenberg F, Widmer D, Bednorz J G, Spreiter R, Bosshard Ch and Günter P 1998 *Acta Crystallogr.* B **54** 399
[14] Shanthi N and Sarma D D 1998 *Phys. Rev.* B **57** 2153
[15] Krause M O and Oliver J H 1979 *J. Phys. Chem. Ref. Data* **8** 329
[16] Mårtensson N and Nyholm R 1981 *Phys. Rev.* B **24** 7121